water penetrated further north. The reduction of thermohaline circulation was caused by a warming and freshening of the North Atlantic and Arctic. This led to a decrease of North Atlantic deep water density and a reduction of the density gradient between the North and South Atlantic, which controls the intensity of meridional overturning (*27*). While the warming of the North Atlantic is the result of nonlinear interaction between vegetation–albedo and sea ice–albedo feedbacks, as discussed above, the freshening of the North Atlantic is a consequence of an intensification of the hydrological cycle in the Northern Hemisphere and an increase in runoff from the continents, which enhances the freshwater flux into the North Atlantic by 0.05 Sv. Because of the weakening of thermohaline circulation, up to 0.1 PW less heat is transported from the South to the North Atlantic, which produces a negative feedback for the Northern Hemisphere warming, but raises the Southern Hemisphere temperature by 0.7°C in the annual mean. The warming reached maximum values of more than 2°C near the Antarctic (Fig. 2B), due to an amplification of temperature changes caused by a reduction of the area of sea ice (Table 1). Paleodata (*28*, *29*) support the possibility of an Antarctic and southern ocean during the mid-Holocene that was up to 2°C warmer than at present.

Our results suggest that during the mid-Holocene, the following three regions were strongly affected by processes related to changes in the vegetation structure and in the oceans. (i) High northern latitudes: A northward expansion of boreal forest due to summer warming leads to an annual warming via the vegetation–snow–albedo feedback, strongly amplified by the sea ice–albedo feedback. (ii) Subtropics: Strong positive feedback between vegetation and precipitation in the subtropics leads to a greening of the Sahara. Major precipitation changes are due to interactive vegetation, while the role of changes in oceanic temperature is ambiguous. (iii) Atlantic: Strong warming of the North Atlantic, together with an increased freshwater flux into the Atlantic basin, leads to a weakening of the thermohaline circulation, which in turn results in a warming of the Southern Hemisphere.

In conclusion, our results reveal strong synergistic effects between the different climate subsystems. They also offer an explanation of how vegetation changes may promote changes in the ocean circulation, thereby leading to a global response connecting both hemispheres. Our results, by and large, agree with paleoclimatic reconstructions. Results from this rather coarse-scale climate-system model provide guidance in the interpretation of past climates. Simulations using comprehensive climate system models in combination with analysis of paleodata are needed to obtain more detailed pictures of the paleoclimate.

REFERENCES AND NOTES

1. T. Webb III, P. J. Bartlein, S. P. Harrison, K. H. Anderson, *Global Climates Since the Last Glacial Maximum*, H. E. Wright *et al.*, Eds. (Univ. of Minnesota Press, Minneapolis, MN, 1993), chap. 17.
2. TEMPO Members, *Global Biogeochem. Cycles* **10**, 727 (1996).
3. I. C. Prentice, J. Guiot, B. Huntley, D. Jolly, R. Cheddadi, *Clim. Dyn.* **12**, 185 (1996).
4. R. Cheddadi, G. Yu, S. P. Harrison, I. C. Prentice, *ibid.* **13**, 1 (1997).
5. V. A. Klimanov and A. A. Velichko, *Atlas of Paleoclimates and Paleoenvironments of the Northern Hemisphere. Late Pleistocene–Holocene*, B. Frenzel, M. Pesci, A. A. Velichko, Eds. (Gustav Fischer, Stuttgart, Germany, 1992).
6. R. A. Monserud, O. V. Denissenko, N. M. Tchebakova, *Clim. Res.* **3**, 143 (1993).
7. G. Yu and S. P. Harrison, *Clim. Dyn.* **12**, 723 (1996).
8. F. A. Street and A. T. Grove, *Quat. Res.* **12**, 83 (1979).
9. D. Jolly, S. P. Harrison, B. Damnati, R. Bonnefille, *Quat. Sci. Rev.*, in press.
10. P. Hoelzmann *et al.*, *Global Biogeochem. Cycles* **12**, 35 (1998).
11. N. de Noblet, P. Braconnot, S. Joussaume, V. Masson, *Clim. Dyn.* **12**, 589 (1996).
12. C. D. Hewitt and J. F. B. Mitchell, *J. Clim.* **9**, 3505 (1996).
13. S. Lorenz, B. Grieger, P. Helbig, K. Herterich, *Geol. Rundsch.* **85**, 513 (1996).
14. N. M. J. Hall and P. J. Valdes, *J. Clim.* **10**, 3 (1997).
15. J. A. Foley, J. E. Kutzbach, M. T. Coe, S. Levis, *Nature* **371**, 52 (1994).
16. J. E. Kutzbach, G. Bonan, J. A. Foley, S. P. Harrison, *ibid.* **384**, 623 (1996).
17. M. Claussen and V. Gayler, *Global Ecol. Biogeogr. Lett.* **6**, 369 (1997).
18. D. Texier *et al.*, *Clim. Dyn.* **13**, 865 (1997).
19. J. E. Kutzbach and Z. Liu, *Science* **278**, 440 (1997).
20. C. D. Hewitt and F. B. Mitchell, *Geophys. Res. Lett.* **25**, 361 (1998).
21. A. Ganopolski, S. Rahmstorf, V. Petoukhov, M. Claussen, *Nature* **391**, 351 (1998).
22. V. Petoukhov *et al.*, *PIK Rep. No. 35* (Potsdam-Institut für Klimafolgenforschung, Potsdam, Germany, 1998).
23. V. Brovkin, A. Ganopolski, Y. Svirezhev, *Ecol. Model.* **101**, 251 (1997).
24. A. L. Berger, *J. Atmos. Sci.* **35**, 2362 (1978).
25. COHMAP Members, *Science* **241**, 1043 (1988).
26. M. T. Coe and G. B. Bonan, *J. Geophys. Res.* **102**, 11087 (1997).
27. S. Rahmstorf, *Clim. Dyn.* **12**, 799 (1996).
28. J. Jouzel *et al.*, *Nature* **329**, 403 (1987).
29. J. D. Hays, J. Imbrie, N. J. Shackleton, *Science* **194**, 1121 (1976).

30. We thank S. Rahmstorf, Potsdam-Institut für Klimafolgenforschung (PIK), and the anonymous reviewers for constructive comments, and A. Schlums, PIK, for editing our manuscript.

11 March 1998; accepted 12 May 1998

Planar Patterned Magnetic Media Obtained by Ion Irradiation

C. Chappert, H. Bernas, J. Ferré, V. Kottler, J.-P. Jamet, Y. Chen, E. Cambril, T. Devolder, F. Rousseaux, V. Mathet, H. Launois

By ion irradiation through a lithographically made resist mask, the magnetic properties of cobalt-platinum simple sandwiches and multilayers were patterned without affecting their roughness and optical properties. This was demonstrated on arrays of 1-micrometer lines by near- and far-field magnetooptical microscopy. The coercive force and magnetic anisotropy of the irradiated regions can be accurately controlled by the irradiation fluence. If combined with high-resolution lithography, this technique holds promise for ultrahigh-density magnetic recording applications.

Among the methods proposed to increase the data storage density in magnetic recording media well beyond expected limits (*1*, *2*), media patterning (*3*, *4*) by appropriate nanometer scale techniques (*5*–*8*) is particularly attractive. The latter will also be required in the field of magnetoelectronics (*9*), with potential applications for new magnetic submicron devices: read head, memory cells, and so forth. To implement a patterning technique, however, several major problems must be solved. First, the patterning process should allow control of the magnetization reversal properties of the submicron element that constitutes the bit or the sensor. Second, medium planarity is crucial. This is related, for instance, to the nanometer scale head-to-media clearance in present day hard-disk technology [as well

C. Chappert, V. Kottler, T. Devolder, V. Mathet, Institut d'Electronique Fondamentale, Unité de Recherche Associée CNRS 022, Université Paris Sud, 91405 Orsay Cedex, France.
H. Bernas, Centre de Spectrométrie Nucléaire et de Spectrométrie de Masse, Unité Propre de Recherche CNRS 6412, Université Paris Sud, 91405 Orsay Cedex, France.
J. Ferré and J.-P. Jamet, Laboratoire de Physique des Solides, Unité de Recherche Associée CNRS 02, Université Paris Sud, 91405 Orsay Cedex, France.
V. Kottler, Y. Chen, E. Cambril, F. Rousseaux, H. Launois, Laboratoire de Microstructures et de Microélectronique, Unité Propre de Recherche CNRS 020, 196 Avenue H. Ravera, BP 107, 92225 Bagneux Cedex, France.

as in future near-field techniques (*10–12*)]. Also, for magnetooptical media, abrupt optical index changes must be avoided to minimize detrimental polarization-dependent diffraction effects (*13, 14*). Planarization thus could play a critical role for magnetic recording technologies, just as it did in semiconductor technologies.

We have devised a method that allows magnetic patterning of a continuous magnetic film without significant modification of the surface roughness or of the film's optical indices. The method is demonstrated here by combining ion irradiation of Co-Pt multilayers with standard e-beam lithography. Arrays of adjacent 1-μm-wide lines with differing magnetic properties were produced and characterized by both far- and near-field magnetooptical microscopy. A crucial feature of the method is that the magnetic parameter changes are induced by a low density of displaced atoms provided by light ion irradiation (*15*) and thus can be precisely adjusted by varying the irradiation fluence, as shown below. When combined with state-of-the-art lithography techniques, the method should ultimately allow nanometer-scale patterning of magnetic properties while preserving ultrasmooth surfaces, which is a major prerequisite for high-density information storage.

Pt-Co-Pt sandwiches and $(Pt\text{-}Co)_n$-Pt multilayers were grown by sputtering at room temperature on either polished fused silica (Herasil) platelets or thermally oxidized SiO_2 (90 nm)-Si (100) wafers (*16–18*). Our own roughness measurements, and published results on similar samples (*19*), demonstrate good film continuity with little intermixing of Co and Pt. Our Pt-Co-Pt sandwiches are ferromagnetic at room temperature from Co thickness t_{Co} = 0.35 nm and have a perpendicular easy magnetization axis up to t_{Co} = 1.2 nm, with perfectly square perpendicular hysteresis loops below t_{Co} = 1 nm (measured via the polar magnetooptical Kerr effect). In this thickness range, magnetization reversal is dominated by easy domain wall propagation (*17*), indicating a low density of wall pinning defects (*20*).

Irradiation parameters were based on prior studies (*15*) of the initial stages of ion-beam mixing in the low-displacement density regime. We used He^+ ions at energies varying from 20 to 100 keV (the results presented below were obtained at 30 keV), with fluences between 2×10^{14} and 2×10^{16} ions per square centimeter. Under these conditions, all He^+ ions stop in the substrate (well below the Co and Pt films). Far less than one displacement per incoming ion is effective for mixing at the Co-Pt interfaces (*15, 21*).

Irradiation of Pt-Co (0.5 nm)-Pt samples at room temperature resulted in perfectly square perpendicular hysteresis loops (Fig. 1) for fluences below 10^{16} ions per square centimeter, as the coercivity progressively decreased from about 200 Oe for the as-grown film down to zero with increasing fluence. Coercive fields as low as a few oersteds could be obtained reproducibly in a perfectly controlled way. Magnetooptical microscopy experiments confirm that magnetization reversal still takes place by easy wall propagation (*20*) at room temperature, as in the as-grown samples. The perpendicular magnetic anisotropy is strongly reduced, with the first anisotropy field, H_{A1}, falling from 11.5 kOe (as-grown sample) to 1.3 kOe after a fluence of 10^{16} ions per square centimeter. Simultaneously, the Kerr rotation θ_K is slightly reduced. Hysteresis loop measurements versus temperature show that this is primarily due to a strong irradiation-induced decrease of the Curie temperature T_c, which is lowered to 60°C at 10^{16} ions per square centimeter. At higher irradiation fluences the samples become paramagnetic at room temperature. Note that, to measure T_c, the irradiated samples were reversibly cycled up to 80°C without any detectable change in the irradiation-induced properties.

The T_c of the as-grown sample is far above 120°C, too high to be measured without damaging the samples. Annealing an as-grown sample at 160°C for 30 min drastically increases the coercivity, strongly reducing θ_K. Furthermore, the loop becomes rounded, evidencing a magnetization reversal mechanism change from easy wall propagation to wall pinning and progressive nucleation (*20*).

The influence of irradiation also depends on t_{Co}. For samples with t_{Co} = 1 nm—that is, just below the spin reorientation transition—30-keV He^+ ion irradiation with fluences as low as 6×10^{15} ions per square centimeter triggers a change to in-plane magnetization (but with no detectable decrease of θ_K). Conversely, no change in the magnetic properties of samples with t_{Co} = 0.8 nm was detected even at fluences up to 10^{16} ions per square centimeter.

Finally, no evidence of irradiation-induced surface roughness was found by atomic force microscopy (AFM) measurements.

As established in (*15*), the effect of irradiation on interfaces such as those of the Co-Pt system may be summarized as follows. Under our specific irradiation conditions, (i) there are no displacement cascades; and (ii) the number of recoil atoms at the film interfaces is very low, and their average distance from their initial position is typically a few interatomic distances. Given some room temperature mobility and in the absence of athermal Frenkel pair recombination, such atoms stand a good chance of finding a lattice site from which they can relax to a stable position whose local surroundings differ from their initial one. Because of their high heats of mixing (*22*), the resulting short-range order around Co can be that of any of several compounds in the Co-Pt phase diagram, and the likelihood of producing a more Pt-rich environment (with weaker magnetic properties) is enhanced. The thinner Co-layer samples (t_{Co} = 0.5 nm) essentially comprise only interfaces, so that all the Co atoms are involved. This explains the strong T_c decrease with irradiation. In the thicker samples, the small recoil range limits the effect to the interface properties, whereas T_c remains high because of the pure Co planes inside the film. For t_{Co} = 1 nm, just below the spin reorientation transition, a very small interface anisotropy reduction suffices to trigger in-plane anisotropy, whereas for t_{Co} = 0.8 nm the effect is very weak. In contrast, annealing at 160°C first affects macroscopic defects such as grain boundaries (thus, for example, increasing the coercive field by creating strong pinning sites) instead of inducing interface changes that occur only at higher temperatures in the Co-Pt system.

The observation that, for t_{Co} = 0.5 nm, the magnetization reversal still occurs through free-wall propagation after irradiation agrees with this interpretation. The resulting structural defects or inhomogeneities are too small to affect domain wall motion and presumably are averaged out by much larger domain wall widths resulting from reduced anisotropy near T_c. This is no longer true at low temperature: below 100 K, irradiated films showed strong pinning effects that were absent in as-grown films.

In extending our study to multilayers, we tested two different structures with identical Co thickness t_{Co} (0.3 nm) and number of periods (six) but differing in Pt interlayer

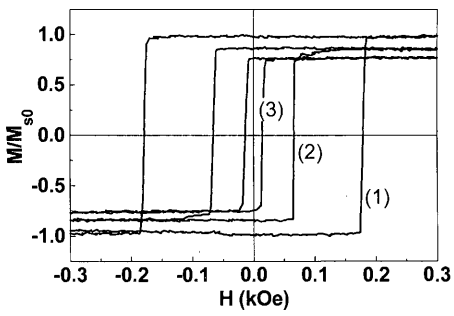

Fig. 1. Hysteresis loops of a Pt-Co (0.5 nm)-Pt-Herasil simple sandwich versus irradiation fluence (He^+ ions, 30 keV). (1) As-grown sample; (2) 3×10^{15} ions per square centimeter; (3) 10^{16} ions per square centimeter. Magnetization M of all curves has been normalized to the saturation magnetization M_{SO} of the as-grown sample.

thickness t_{Pt} (0.6 and 1.4 nm). The discussion above also applies here, but we now must consider the interaction between magnetic layers, which is known to be ferromagnetic in the Co-Pt system because of Pt spin polarization. In as-grown samples, this results in much stronger ferromagnetism than in simple sandwiches, with square perpendicular loops and high coercive fields (Fig. 2).

Irradiation of the sample with t_{Pt} = 1.4 nm leads to perfectly square perpendicular hysteresis loops (Fig. 2) for fluences below 6×10^{15} ions per square centimeter, but the coercive field progressively decreases with increasing fluence as for the t_{Co} = 0.5 nm simple sandwich (Fig. 1). At a fluence of 6×10^{15} ions per square centimeter the tilted loop with nonzero remnant magnetization indicates the spontaneous formation of up-down magnetic domains (*18*). At higher fluences, the loops are typical of an easy plane magnetization axis (note that θ_K remains unchanged). The sample with t_{Pt} = 0.6 nm displays very similar behavior, but the magnetization reorientation occurs at only 3×10^{15} ions per square centimeter.

As discussed above, irradiation changes the Pt concentration profile at each Co layer interface (and therefore the short-range order around interface Co atoms). But in contrast to the single film case, the existence of strong interlayer coupling keeps T_c high (this is confirmed by the fact that θ_K remains constant), while the perpendicular anisotropy is reduced. The interlayer coupling might even increase if interdiffusion increased the spin polarization in the Pt layer. Hence, the sample behavior evolves from that of the familiar Co-Pt multilayer with perpendicular anisotropy toward that of a thin Co-Pt alloy ferromagnetic film with in-plane anisotropy.

These results suggest the exciting possibility of locally changing the magnetic properties of a sample by using a technique similar to that of semiconductor doping (irradiation through a lithographically defined mask).

A Pt-Co (0.5 nm)-Pt simple sandwich and a $[Pt\text{-}Co]_6$ multilayer with t_{Co} = 0.3 nm and t_{Pt} = 1.4 nm were produced, on which arrays of 1-μm wires separated by 1 μm were defined by e-beam lithography in a 0.85-μm-thick poly(methyl methacrylate) PMMA resist layer. Both samples were irradiated with 30-keV He^+ ions through the resist mask, which was then removed in a hot trichloroethane bath, followed by short exposure to an oxygen plasma to remove the PMMA residues (which occur mostly at the boundaries of the irradiated areas). The samples were studied by magnetooptical microscopy, either in the far-field (*20*) or in the near-field transmission mode (*14*).

The simple sandwich was irradiated at a fluence of 10^{16} ions per square centimeter, high enough to make the irradiated area paramagnetic at room temperature in this particular sample. A magnetic domain (Fig. 3A, white area), nucleated well outside the image and expanding in a nonirradiated region of the sample (top half of the image), meets the limit with the "magnetically patterned" array. The domain wall rapidly propagates toward the left in the unpatterned region and penetrates the array through the nonirradiated stripes (Fig. 3B). Note that the propagation velocity is not exactly the same in all stripes (there is obviously a distribution of pinning sites).

The multilayer was irradiated at a dose of 2×10^{15} ions per square centimeter, which is expected to halve the coercive field in the irradiated area (see Fig. 2). The optical transmission image (Fig. 4A) shows no contrast, leading to near-field magnetic images with negligible diffraction effects on the magnetically saturated sample (Fig. 4B). As a result of the local coercivity change induced by irradiation, we could reverse the magnetization of the irradiated areas alone (Fig. 4C) while preserving good magnetic contrast.

Beam-induced magnetic patterning allows us to create adjoining regions with very different magnetic properties, such as perpendicular versus in-plane magnetization or paramagnetic or stripe domain structures in otherwise smooth and optically uniform films. The method demonstrated here can be extended to submicron sizes (*23*) and to other materials whose magnetic properties are sensitive to irradiation (*24*).

This should provide exciting possibilities for studying magnetic configurations and magnetization reversal processes in patterned structures, with little or no influence of the defects encountered in etched structures. If our estimates of the ultimate obtainable resolutions (*23*) are confirmed experimentally, the method holds promise for ultrahigh density magnetic recording appli-

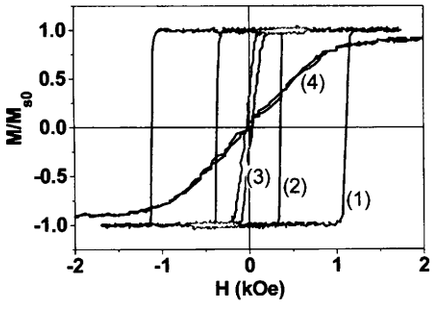

Fig. 2. Hysteresis loop of a Pt-[Pt (1.4 nm)-Co (0.3 nm)]$_6$-Pt-Herasil multilayer versus irradiation fluence (He^+ ions, 30 keV). (1) As-grown sample; (2) 2×10^{15} ions per square centimeter; (3) 6×10^{15} ions per square centimeter; (4) 10^{16} ions per square centimeter. Magnetization M of all curves has been normalized to the saturation magnetization M_{SO} of the as-grown sample.

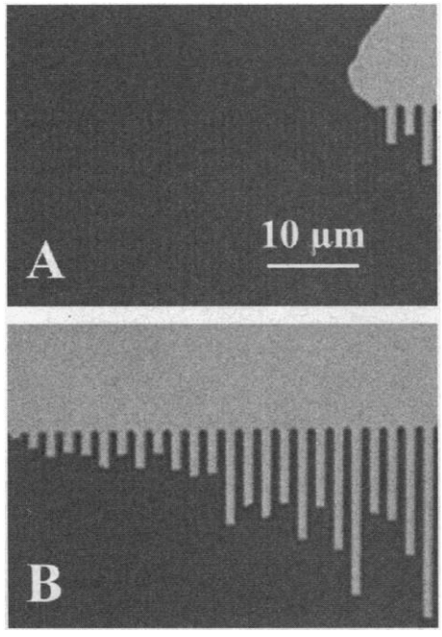

Fig. 3. Image in far-field magnetooptical microscopy of an array of stripes 1 μm wide, separated by 1 μm, magnetically patterned in a Pt-Co (0.5 nm)-Pt-Herasil simple sandwich. The sample was irradiated with 30-keV He^+ ions at a dose of 10^{16} ions per square centimeter, through a mask of PMMA resist defined by e-beam lithography. In this specific sample, this made the unprotected areas paramagnetic at room temperature. Images (**A**) and (**B**) are both differences from a magnetically saturated image, and the reversed domains appear in white. A pulse of magnetic field of amplitude 82 Oe and duration 2 s was applied between (A) and (B).

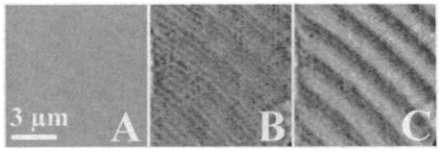

Fig. 4. Images in near-field magnetooptical microscopy of an array of stripes 1 μm wide, separated by 1 μm, magnetically patterned in a Pt-[Pt (1.4 nm)-Co (0.3 nm)]$_6$-Pt-Herasil multilayer. The sample was irradiated with 30-keV He^+ ions at a dose of 2×10^{15} ions per square centimeter, through a mask of PMMA resist defined by e-beam lithography, reducing the coercivity of the unprotected areas by a factor greater than 2 (see Fig. 2). (**A**) Optical transmission image (without polarization analysis). (**B**) Magnetooptical image of the magnetically saturated array. The faint contrast is due to residual PMMA before exposure to oxygen plasma. (**C**) Magnetooptical image of the array after reversal of the magnetization in the irradiated area only (white stripes). Magnetic resolution of our experiment was about 200 nm.

cations (*10–12*) or for fabrication of integrated magnetic memory devices or sensors (*25*). It could also be of interest for ultrahigh density near-field optical recording (*26, 27*), because optical properties also may be locally changed by adjusting the irradiation conditions.

REFERENCES AND NOTES

1. E. Grochowski and D. A. Thompson, *IEEE Trans. Magn.* **MAG-30**, 3797 (1994).
2. D. N. Lambeth, E. M. T. Velu, G. H. Bellesis, L. L. Lee, D. E. Laughlin, *J. Appl. Phys.* **79**, 4496 (1996).
3. S. Gadetsky, J. K. Erwin, M. Mansuripur, *ibid.*, p. 5687 (1996).
4. S. Y. Chou, M. S. Wei, P. R. Krauss, P. Fischer, *ibid.* **76**, 6673 (1994).
5. S. Y. Chou, P. R. Krauss, P. J. Renstrom, *Science* **272**, 85 (1996).
6. Y. Xia, X. M. Zhao, G. M. Whitesides, *Microelecton. Eng.* **32**, 255 (1996).
7. Y. Chen *et al.*, *J. Vac. Sci. Technol. B* **12**, 3959 (1994).
8. A. Fernandez, P. J. Bedrossian, S. L. Baker, S. P. Vernon, D. R. Kania, *IEEE Trans. Magn. Mag.* **32**, 4472 (1996).
9. J. L. Simonds, *Phys. Today* **48** (no. 4), 26 (1995).
10. E. Betzig *et al.*, *Appl. Phys. Lett.* **61**, 142 (1992).
11. B. D. Terris, H. J. Mamin, D. Rugar, W. R. Studenmund, G. S. Kino, *ibid.* **65**, 388 (1994).
12. T. J. Silva, S. Schultz, D. Weller, *ibid.*, p. 658.
13. M. Mansuripur, *The Physical Principles of Magneto-Optical Recording* (Cambridge Univ. Press, Cambridge, 1995).
14. V. Kottler, N. Essaidi, N. Ronarch, C. Chappert, Y. Chen, *J. Magn. Magn. Mater.* **165**, 398 (1997); V. Kottler, C. Chappert, N. Essaidi, Y. Chen, *IEEE Trans. Magn.*, in press.
15. M. G. Le Boité, A. Traverse, L. Névot, B. Pardo, J. Corno, *J. Mater. Res.* **3**, 1089 (1988); M. G. Le Boité, A. Traverse, H. Bernas, C. Janot, J. Chevrier, *Mater. Lett.* **6**, 173 (1988); A. Traverse, M. G. Le Boité, G. Martin, *Europhys. Lett.* **8**, 633 (1989).
16. After a soft radio frequency (rf) etch of the substrate, a 6.5-nm-thick Pt buffer layer is first deposited at about 0.25 nm/s using dc magnetron (at an Ar pressure of 5×10^{-3} mbar), which gives a flat continuous polycrystalline film with nearly perfect (111) texture and small (~7 nm) grain size. Then rf diode and rf magnetron, respectively, are used for deposition of the Co and Pt layers at around 0.02 nm/s, terminating all samples with a 3.4-nm Pt coverage layer. AFM measurements show a root mean square roughness of the Pt buffer layer around 0.2 nm, which is preserved on the topmost surface (Pt coverage layer) for all samples.
17. S. Lemerle *et al.*, in *Magnetic Hysteresis in Novel Magnetic Materials, NATO ASI Series E: Applied Sciences–338*, G. C. Hadjipanayis, Ed. (Kluwer Academic, Dordrecht, Netherlands, 1997), pp. 537–542.
18. L. Belliard *et al.*, *J. Appl. Phys.* **81**, 5315 (1997).
19. J. P. Deville, A. Barbier, C. Boeglin, B. Carrière, *Mater. Res. Soc. Symp. Proc.* **313**, 519 (1993).
20. J. Pommier *et al.*, *Phys. Rev. Lett.* **65**, 2054 (1990).
21. J. Ziegler, J. Biersack, U. Littmark, *The Stopping and Range of Ions in Solids* (Pergamon, New York, 1985).
22. T. Massalski, *Binary Alloy Phase Diagrams* (Metals Information Society, Metals Park, OH, ed. 2, 1990).
23. We have not yet studied these limits experimentally but have performed simulations (T. Devolder *et al.*, unpublished data) to determine the length (hereafter called "transition length") over which ion-induced structural changes occur at a mask edge. The limiting factor of the transition length is not the ion beam angular spread but the ion beam lateral straggling values at the Pt-Co layer depth, which in turn depend on the mask thickness seen by the ion beam in case of incomplete stopping. To determine the effect of a lithographically made irradiation mask on the transition length, we performed calculations for a PMMA stripe (200 nm wide, 600 nm high, with both a vertical- and a pyramid-based edge profile deduced from scanning electron micrographs of real masks). Transition length estimates were obtained by convoluting mask shapes corresponding to our experimental conditions with lateral straggling values deduced from TRIM simulations (*19*). Depending on the exact shapes assumed for the former, the obtainable lateral resolution for PMMA masks varied from 100 nm (worst case) to 20 nm (best case). We anticipate that even lower values (down to about 5 nm or less) might be obtained by using more appropriate masks and patterning techniques; see, for example, [R. M. H. New, R. F. W. Pease, R. L. White, *J. Vac. Sci. Technol.* B **12**, 3196 (1994)]. The fact that the magnetic property changes are not related in a simple way to the ion-induced structural changes must be considered. In separate studies (unpublished data) of unmasked Co-Pt structures, we determined the ion fluence dependence of the Kerr rotation and the anisotropy, from which we can estimate the transition length for magnetic property changes. We find that in most cases the magnetic transition will be sharper than the structural one.
24. M. Cai *et al.*, *J. Appl. Phys.* **81**, 5200 (1997).
25. M. Johnson *et al.*, *Appl. Phys. Lett.* **71**, 974 (1997).
26. B. D. Terris, H. J. Mamin, D. Rugar, *ibid.* **68**, 141 (1996).
27. Y. Martin, S. Rishton, H. K. Wickramasinghe, *ibid.* **71**, 1 (1997).

28. We thank O. Kaitasov and S. Gautrot for technical assistance. This work was performed within the framework of the ISARD collaboration (Université Paris–Sud). V. K. is funded by a Marie-Curie grant from the European Union.

1 December 1997; accepted 29 April 1998

Post-Cambrian Trilobite Diversity and Evolutionary Faunas

Jonathan M. Adrain,* Richard A. Fortey, Stephen R. Westrop

A cluster analysis of the stratigraphic distribution of all Ordovician trilobite families, based on a comprehensive taxonomic database, identified two major faunas with disjunct temporal diversity trends. The Ibex Fauna behaved as a cohort, declining through the Ordovician and disappearing at the end-Ordovician mass extinction. In contrast, the Whiterock Fauna radiated rapidly during the Middle Ordovician and gave rise to all post-Ordovician trilobite diversity. Its pattern of diversification matches that of the Paleozoic Evolutionary Fauna; hence, trilobites were active participants in the great Ordovician radiations. Extinction patterns at the end of the Ordovician are related to clade size: Surviving trilobite families show higher genus diversity than extinguished families.

Trilobites are among the most common fossils of the Early Paleozoic, and an understanding of their history is central to any hypothesis of the development of the marine biosphere during this time. Cumulative trilobite diversity (*1*) is often portrayed as a bottom-heavy spindle diagram derived by counting genera or families recognized during particular epochs. The most current description of cumulative taxonomic diversity is Sepkoski's compendium of marine families (*2*) and genera (*3*) and his seminal factor-analytical description of the marine record (*4*). We used a new comprehensive genus-level global data set to reinvestigate patterns of post-Cambrian trilobite diversity.

Trilobite diversity has been understood in relation to three major events in the Early Phanerozoic history of life: the Cambrian explosion (*5*), the Ordovician radiation (*6*), and the end-Ordovician mass extinction (*7*). Of these events, the diversity pattern of trilobites after the Cambrian explosion is uncontroversial; with the advent of mineralized hard parts, trilobites radiated rapidly and soon reached their peak clade diversity (*8*). The role of trilobites in the Ordovician events is less well understood. The class was in modest decline during the time of the Ordovician radiation (*1, 3, 4*), along with other elements of the Cambrian Evolutionary Fauna (*4*). Trilobites were one of the groups most affected by the end-Ordovician extinction, and most estimates record a loss of about half of familial or generic diversity at this event (*3, 4*). Post-Cambrian trilobite history has therefore been inferred to follow a general and sustained decline, or a decay of a high-diversity Early Ordovician cohort (*9*). However, the cumulative diversity curve poorly reflects some important features of trilobite history: (i) No natural subgroup of trilobites (monophyletic order, superfamily, or family) has an Ordovician-Silurian diversity history matching the shape of the cumulative plot. Although components may have different diversity histories from cumulative trends, no clade among the trilobites is even similar to the curve for the Ibex (Lower Ordovician) through Wenlock (Silurian) series.

J. M. Adrain and R. A. Fortey, Department of Palaeontology, Natural History Museum, Cromwell Road, London SW7 5BD, UK.
S. R. Westrop, Oklahoma Museum of Natural History and School of Geology and Geophysics, University of Oklahoma, Norman, OK 73019, USA.

*To whom correspondence should be addressed. E-mail: j.adrain@nhm.ac.uk